Single-channel Ca^{2+} imaging implicates Aβ1–42 amyloid pores in Alzheimer's disease pathology

Angelo Demuro,[1] Martin Smith,[1] and Ian Parker[1,2]

[1]Department of Neurobiology and Behavior and [2]Department of Physiology and Biophysics, University of California, Irvine, Irvine, CA 92697

Oligomeric forms of Aβ peptides are implicated in Alzheimer's disease (AD) and disrupt membrane integrity, leading to cytosolic calcium (Ca^{2+}) elevation. Proposed mechanisms by which Aβ mediates its effects include lipid destabilization, activation of native membrane channels, and aggregation of Aβ into Ca^{2+}-permeable pores. We distinguished between these using total internal reflection fluorescence (TIRF) microscopy to image Ca^{2+} influx in *Xenopus laevis* oocytes. Aβ1–42 oligomers evoked single-channel Ca^{2+} fluorescence transients (SCCaFTs), which resembled those from classical ion channels but which were not attributable to endogenous oocyte channels. SCCaFTs displayed widely variable open probabilities (P_o) and stepwise transitions among multiple amplitude levels reminiscent of subconductance levels of ion channels. The proportion of high P_o, large amplitude SCCaFTs grew with time, suggesting that continued oligomer aggregation results in the formation of highly toxic pores. We conclude that formation of intrinsic Ca^{2+}-permeable membrane pores is a major pathological mechanism in AD and introduce TIRF imaging for massively parallel single-channel studies of the incorporation, assembly, and properties of amyloidogenic oligomers.

Introduction

A seminal event in the pathogenesis of Alzheimer's disease (AD) is the abnormal proteolytic processing of amyloid precursor protein (APP), resulting in increased production of a self-aggregating form of β amyloid (Aβ). Mutations in APP and in presenilins (secretase enzymes involved in APP processing) that are linked to early-onset familial forms of AD cause excessive production of Aβ, resulting in massive accumulation of fibrillar Aβ in the amyloid plaques that are a hallmark of brains from AD patients (Cras et al., 1991). For many years, the plaques were thought to be the primary culprit of AD pathology, as formulated by the amyloid hypothesis (Hardy and Higgins, 1992). However, that hypothesis fails to explain several important pathological and clinical characteristics of AD. Markedly, there is little correlation between the amounts of fibrillar Aβ deposit at autopsy and the clinical severity of AD (Lemere et al., 1996). In contrast, a good correlation has been found between early cognitive dysfunction and levels of soluble forms of Aβ in the brain (Jensen et al., 2000; Shankar et al., 2008).

Aggregation of Aβ proceeds through several steps, including the formation of soluble low molecular weight spherical oligomers, before assuming a final and stable conformation as the insoluble fibrils from which plaques are constituted (Bucciantini et al., 2002; Kayed et al., 2003; Glabe, 2004). Growing evidence suggests that the neurotoxicity is associated with soluble aggregates of Aβs rather than with the plaques themselves (Walsh et al., 2002; Kayed et al., 2003; Demuro et al., 2005; Deshpande et al., 2006). Moreover, soluble oligomeric forms of amyloidogenic peptides associated with diseases including Huntington's and Parkinson's have been shown to be similarly toxic, and this toxicity is directly related to the morphological structure of the aggregates rather than to their protein sequence (Kayed et al., 2003; Demuro et al., 2005). Consistent with this, antibodies raised against Aβ peptides in their oligomeric form recognize oligomeric species of other amyloidogenic proteins (α-synuclein, polyglutamin, and lysozime) but not the monomeric or the fibrillar forms of Aβ and other peptides (Kayed et al., 2003).

Amyloid oligomers, but not monomers, exert a common pathophysiological action in disrupting the integrity of cell membranes, resulting in uncontrolled influx of extracellular Ca^{2+}

Correspondence to Angelo Demuro: ademuro@uci.edu

Abbreviations used in this paper: AD, Alzheimer's disease; APP, amyloid precursor protein; SCCaFT, single-channel Ca^{2+} fluorescence transient; TIRF, total internal reflection fluorescence.

The Rockefeller University Press $30.00
J. Cell Biol. Vol. 195 No. 3 515–524
www.jcb.org/cgi/doi/10.1083/jcb.201104133

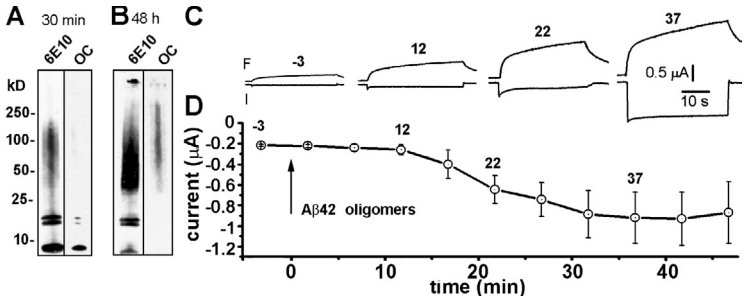

Figure 1. **Western blot analysis of Aβ1−42 oligomer preparations and assay of potency to evoke Ca^{2+} influx in *Xenopus* oocytes.** (A and B) Western blots showing aggregation profiles of Aβ1–42 at 30 min after initially dissolving Aβ peptide monomer (A) and after 48 h of incubation (B). 4 µg of samples was separated using gel electrophoresis on a 4–20% Tris-HCl gel. The membranes were probed separately with a monoclonal antibody, 6E10, which is sequence specific to Aβ, and with OC antibody, which recognizes a generic epitope associated with the fibrillar amyloid conformation independent of peptide sequence. Black lines indicate that intervening lanes have been spliced out. (C and D) Bioassay of the potency of Aβ1–42 oligomer preparations to induce membrane permeability to Ca^{2+}. The traces in C show representative global Ca^{2+} fluorescence signals (indicated as F; top) and corresponding voltage-clamped membrane currents (indicated as I; bottom) evoked by 30-s voltage steps from 0 to −100 mV delivered at various times (indicated in minutes) before and after pipette application of Aβ1−42 oligomers to a nonpeeled oocyte loaded with fluo-4 dextran. (D) Measurements of inward currents (without leak subtraction) evoked by voltage steps from 0 to −100 mV taken at 5-min intervals after application of Aβ1−42 (final bath concentration of 1 µg/ml). Data show means ± 1 SEM from four oocytes using two different Aβ1−42 oligomer preparations.

with devastating consequences for cellular Ca^{2+} homeostasis (Mattson et al., 1992; Demuro et al., 2005; Deshpande et al., 2006). Major questions remain as to how amyloid oligomers exert their action on the cell membrane, and three distinct mechanisms have been proposed: (1) the fluidizing action hypothesis postulates that Aβ destabilizes membrane integrity via a nonreceptor-mediated mechanism that alters the physicochemical properties of membrane lipids and proteins (Hertel et al., 1997; Mason et al., 1999; Sokolov et al., 2006); (2) Aβ oligomers have been proposed to directly activate endogenous Ca^{2+}-permeable receptor/channels such as neuronal nicotinic and glutamate receptors (Wang et al., 2000; De Felice et al., 2007; Alberdi et al., 2010); and (3) Aβ and other amyloidogenic oligomers are proposed to incorporate into the cell membrane to form pores with high cation conductivity (Arispe et al., 1993; Pollard et al., 1993; Lin et al., 2001; Quist et al., 2005). Evidence in support of the pore-forming mechanism derives from electrophysiological recordings from both artificial and biological membranes (Lin et al., 2001; Lashuel et al., 2002; Quist et al., 2005; Capone et al., 2009) and from theoretical modeling (Durell et al., 1994; Jang et al., 2008). Moreover, EM reveals porelike Aβ structures in cell membranes of postmortem brains from AD but not control patients (Inoue, 2008), and similar Aβ globular structures have been visualized by atomic force microscopy in lipid membranes treated with synthetic Aβ peptides (Lin et al., 2001; Lashuel et al., 2002).

Studies of the molecular mechanisms by which amyloid oligomers induce membrane permeability have largely been confined to electrophysiological recordings of currents across artificial lipid bilayers (Kagan et al., 2004) or excised patches of neuronal membranes (Kawahara et al., 1997). Here, we used a technique (optical patch-clamping) we had previously developed for high-resolution imaging of Ca^{2+} flux through single ligand– and voltage-gated channels (Demuro and Parker, 2004a, 2005a) to study the functioning of individual Aβ1−42 oligomer pores in the plasma membrane of *Xenopus laevis* oocytes, which substantially lack endogenous Ca^{2+} channels (Weber, 1999). We find that extracellular application of Aβ1−42 oligomers induces punctate Ca^{2+} transients that closely resemble the single-channel Ca^{2+} fluorescence transients (SCCaFTs) generated by classical protein membrane channels. The results obtained with this novel approach support a pore-forming mechanism of Aβ toxicity and provide insights into the formation and functional characteristics of Aβ pores.

Results

Aβ oligomers induce Ca^{2+} influx across the oocyte membrane

We had previously shown that application of soluble Aβ oligomers (but not monomers or fibrils) to cultured neuroblastoma cells evoked large increases in cytosolic (Ca^{2+}) that arise largely through Ca^{2+} influx across the plasma membrane (Demuro et al., 2005). Our object here was to study this plasmalemmal Ca^{2+} flux at the single-channel level using total internal reflection fluorescence (TIRF) microscopy of near-membrane Ca^{2+} signals, which we had developed as a technique to resolve the gating of individual ion channels in the membrane of *Xenopus* oocytes (Demuro and Parker, 2005a). The oocyte offers several advantages for study of the actions of Aβ oligomers, including a paucity of native ligand– and voltage-gated channels (Bourinet et al., 1992) that have been proposed to be targets of Aβ modulation in neuronal cells (Wang et al., 2000; De Felice et al., 2007; Alberdi et al., 2010). We chose to investigate the molecular mechanisms of toxicity of the Aβ1–42 peptide, rather than the Aβ1–40 form, in light of the reported correlation between the early onset of familial AD and the increased level of Aβ1–42 in the AD brain (Jarrett and Lansbury, 1993; Kim and Hecht, 2005).

Aβ1–42 oligomers were prepared by incubating aqueous solutions of peptide monomer for up to 48 h. Western blots (Fig. 1, A and B) showed a wide range of oligomeric species with molecular masses ranging between ∼35 and 300 kD, corresponding to roughly 5–40 peptide multimers, which were recognized by 6E10 and OC, sequence- and fibrillar-specific Aβ antibodies, respectively (Kayed et al., 2010). Aβ oligomer preparations were assayed for their ability to induce macroscopic Ca^{2+} influx in oocytes. Fig. 1 C shows representative membrane currents and fluorescence signals in an oocyte loaded with the Ca^{2+} indicator fluo-4 generated in response to voltage-clamped hyperpolarizing pulses from 0 to −100 mV to transiently increase the electrical driving force for Ca^{2+} entry. The pulses initially evoked only a small inward leakage current and a small rise in fluorescence, but both signals increased over

~40 min after adding Aβ1−42 oligomers to the bathing solution (Fig. 1 D), reflecting an increase in membrane Ca^{2+} permeability and consequent activation of a Ca^{2+}-activated Cl^- conductance (Miledi and Parker, 1984). This action was specific to the oligomeric species of Aβ that aggregated after long-term incubation (12–48 h) because application of solutions of Aβ peptide that had been prepared shortly beforehand evoked little or no response.

Imaging Ca^{2+} signals from individual Aβ1−42 pores

To resolve Ca^{2+} influx through individual Aβ pores, oocytes were stripped of the vitelline envelope, allowing the cell membrane to appose closely to the cleaned cover glass of the imaging chamber so that TIRF microscopy of fluo-4 could be used to image Ca^{2+} signals restricted within the ~100-nm-deep evanescent field immediately adjacent to the plasma membrane. We selected regions with uniform background-resting fluorescence close to the edge of the membrane footprint, so as to maximize diffusional access of Aβ. Aβ1−42 oligomers dissolved at 1 μg/ml in Ringer's solution were delivered by superperfusion from a micropipette (30–50-μm tip) within <200 μm of the edge of the imaging field. A total volume of ~3 ml was delivered at 0.3–0.5 ml/min to a chamber initially containing 0.5 ml Ringer's solution.

Before application of Aβ, hyperpolarizing steps to −100 mV usually evoked little or no change in resting fluorescence, and we discarded oocytes showing sustained or transient local Ca^{2+} elevations. In contrast, hyperpolarizing pulses evoked numerous localized, flickering bright spots when examined >20 min after Aβ application (Fig. 2 A). We used a custom software routine (CellSpecks) to locate the positions of these Ca^{2+} hotspots and to automatically generate plots of the fluorescence time course from localized regions of interest. For example, Fig. 2 B presents a representative map of all sites (n = 785) identified within the 40 × 40–μm imaging field during a 20-s hyperpolarization. The inhomogeneous distribution across Fig. 2 B is representative of eight similar experiments and probably reflects gradients of Aβ oligomer concentration away from the application pipette, which was located near the bottom right corner of the imaged region.

Fluorescence signals at individual sites were restricted within ~1 μm and flickered on and off at millisecond timescales (Fig. 2 C), closely resembling both patch-clamp recordings from ion channels and optical recordings of Ca^{2+} flux through Ca^{2+}-permeable voltage- and ligand-gated ion channels (Demuro and Parker, 2003, 2004b, 2005a). In light of this similarity, together with other properties described later, we refer to them as SCCaFTs (Demuro and Parker, 2005a).

Aβ SCCaFTs arise through local influx of Ca^{2+} across the plasma membrane

SCCaFTs induced by Aβ1−42 oligomers disappeared after removal of external Ca^{2+} from the bathing solution (Ringer's solution without added Ca^{2+} plus 3 mM EGTA), consistent with an extracellular source of Ca^{2+}. Moreover, the mean amplitudes of SCCaFTs reduced at more positive membrane potentials

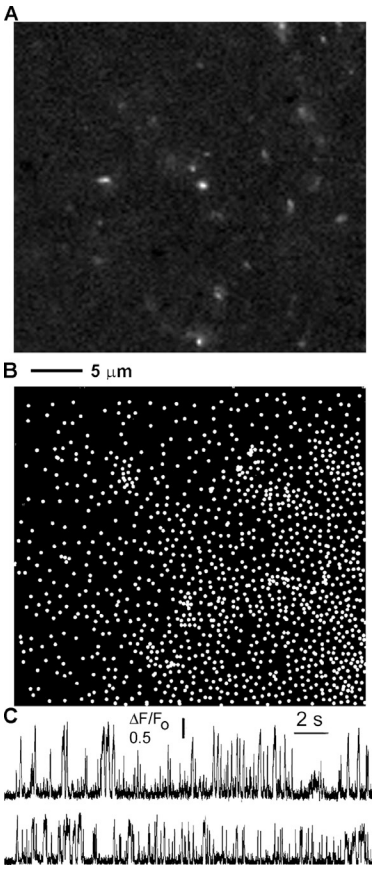

Figure 2. **Aβ1–42 oligomers form Ca^{2+}-permeable ion pores in the plasma membrane of *Xenopus* oocytes.** (A) Representative image showing localized Ca^{2+} transients (SCCaFTs) imaged by TIRF microscopy during hyperpolarization to −100 mV within a 40 × 40–μm region of a vitelline-stripped oocyte loaded with fluo-4 dextran and EGTA. The imaging region was close to the edge of the footprint of the oocyte on the cover glass, and 1 μg/ml Aβ1−42 oligomers was applied to the bathing solution ~18 min beforehand from a pipette positioned near the bottom right corner of the image frame. No activity was observed before application of Aβ1−42. The grayscale image of fluorescence ratio changes ($\Delta F/F_o$; black = 0, white = 1.6) shows a mean of six consecutive video frames (2 ms per frame) from within a sequence of 15,000 frames. (B) Map showing the locations of all SCCaFTs (Aβ pores) identified during a 20-s recording from the membrane region in A. The map was automatically constructed by CellSpecks by identifying the coordinates of each SCCaFT. (C) Representative fluorescence profiles from regions of interest (1 μm^2) centered on two pore locations.

(Fig. 3, A and B), showing a voltage dependence and extrapolated suppression potential (Fig. 3 A) mirroring that of SCCaFTs from Ca^{2+}-permeable nicotinic acetylcholine receptors expressed in the oocyte (Demuro and Parker, 2005a), as expected from the electrical driving force for Ca^{2+} influx.

Zinc ions inhibit the Ca^{2+} conductance induced by Aβ oligomers (Arispe et al., 1996, 2007; Kawahara et al., 1997; Rhee et al., 1998). Application of 300 μM extracellular Zn^{2+} strongly attenuated the appearance of Aβ SCCaFTs (Fig. 3 C), and the mean fluorescence change across 10 × 10–μm membrane regions in response to hyperpolarization reduced ~10-fold from $\Delta F/F_o$ 0.14 ± 0.03 (n = 7 trials) to 0.016 ± 0.002 (n = 4), which is close to the mean value seen in the absence of Aβ (0.013 ± 0.002; n = 6).

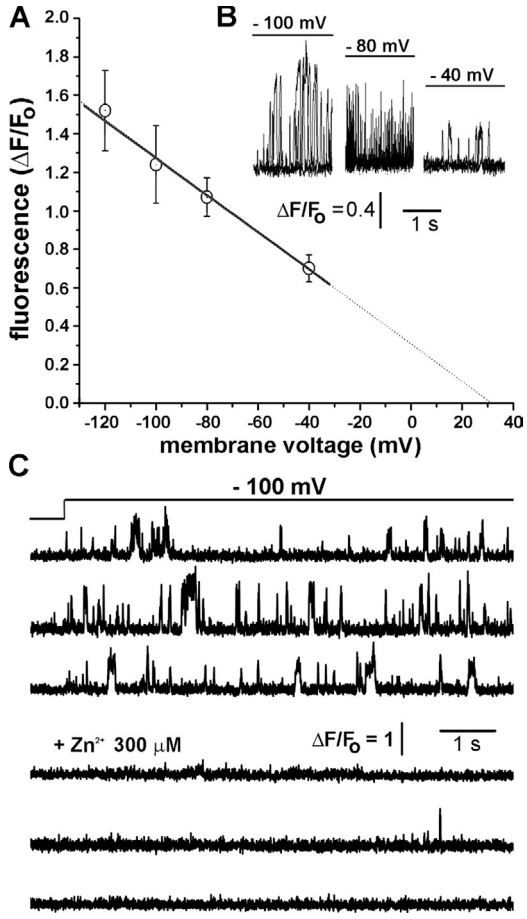

Figure 3. **Ca^{2+} influx through Aβ1−42 pores is voltage dependent and blocked by Zn^{2+}.** (A) Amplitudes of SCCaFTs from Aβ1−42 pores plotted as function of membrane potential. Points show mean amplitudes ($\Delta F/F_0$) ± 1 SEM from >30 events from 10 different pores. The fitted regression line extrapolates to 0 at about 30 mV. (B) Superimposed records of SCCaFTs recorded from 26 Aβ pore sites at the voltages indicated. (C) Representative traces from three regions of interest showing control records of SCCaFTs induced by Aβ1−42 (top) and records from the same regions 5 min after adding 300 µM Zn^{2+} to the bathing solution.

SCCaFTs do not involve Aβ activation of endogenous ion channels in the oocyte membrane

Several studies indicate that Aβ may increase membrane conductance by activating diverse endogenous channels, including voltage-gated Ca^{2+} channels and nicotinic, AMPA, *N*-methyl-D-aspartic acid, and serotonin receptors (Rovira et al., 2002; De Felice et al., 2007; Alberdi et al., 2010). However, it is improbable that the SCCaFTs we observed arose from actions on any of these channels, as they are absent or present only occasionally and at very low density in oocytes (Weber, 1999). The only known Ca^{2+}-permeable channels present at high density in the oocyte membrane are stretch-activated channels and store-operated channels that mediate Ca^{2+} influx after depletion of ER Ca^{2+} (Weber, 1999). Neither is likely to account for our results. Application of 5 µM of the specific stretch-activated channel blocker gsmtx-4 (Bode et al., 2001) failed to significantly inhibit whole-cell currents induced 40 min after application of 1 µg/ml Aβ1–42 oligomers ($n = 3$ oocytes; 2.1 ± 0.51 and 1.85 ± 0.7 µA before and after gsmtx-4, respectively). Moreover, during activation of store-operated influx in oocytes, we observed only a generalized rise in fluorescence Ca^{2+} signal without evidence of discrete SCCaFTs, suggesting that, like Ca^{2+} release–activated Ca^{2+} channels in other cells (Cahalan, 2009), these channels in the oocyte have an extremely low Ca^{2+} conductance, incompatible with our observation of the large SCCaFTs generated by Aβ.

Collectively, these results indicate that TIRF imaging of SCCaFTs provides a means to study the properties of pores directly constituted from Aβ oligomers, an approach with important advantages over electrophysiological techniques such as lipid bilayer reconstitution, in that measurements can be obtained simultaneously and independently from hundreds of pores within the membrane of intact cells.

Single Aβ1−42 pores exhibit multiple Ca^{2+} permeability levels

A characteristic feature of Aβ SCCaFTs was the appearance of stepwise transitions between multiple fluorescence levels (Fig. 4 A). The fluorescence signal recorded by TIRF microscopy closely reflects instantaneous Ca^{2+} flux (Ca^{2+} current) through single channels (Demuro and Parker, 2005a; Smith and Parker, 2009), and the stepwise changes are reminiscent of current recordings from lipid bilayer systems describing interconversion of Aβ1−40 pores between multiple conductance levels (Arispe et al., 2007). To further analyze this behavior, we measured dwell-state fluorescence amplitudes by visual inspection from 76 Aβ pore sites. The resulting multimodal amplitude distribution (Fig. 4 B) revealed several (five or more) peaks, which do not appear to recur at precise integer multiples.

Variability in calcium permeability and gating kinetics among Aβ1−42 pores

In addition to the variability within and between individual SCCaFTs at a given site (e.g., Fig. 4 A), further variation in fluorescence amplitudes was apparent between different pores. We characterized this by using the CellSpecks program to derive the distribution of the maximal event amplitude detected at each of 2,820 sites (Fig. 4 C). A few sites gave SCCaFTs >2 $\Delta F/F_0$, whereas at others, no events larger than ∼0.4 $\Delta F/F_0$ were observed. Moreover, the latter value likely represents an upper bound, owing to the inability of the automated routine to reliably detect yet smaller events.

An even greater variability among Aβ1−42 pores was apparent in their kinetic properties. This is illustrated in Fig. 5 A, showing a channel chip representation (Demuro and Parker, 2005a) of 172 pores presented in order of decreasing open probability (P_o; top to bottom), and in Fig. 5 B, showing representative traces from pores that showed frequent large amplitude SCCaFTs and those that gave only infrequent smaller events. The overall distribution of mean SCCaFT durations among 2,820 pores within a single 40 × 40–µm membrane region was well fitted by a double exponential function with time constants of 5 and 16 ms (Fig. 6 A); the distribution of mean closed times (intervals between successive SCCaFTs) for the same pores fitted a double exponential decay function with time

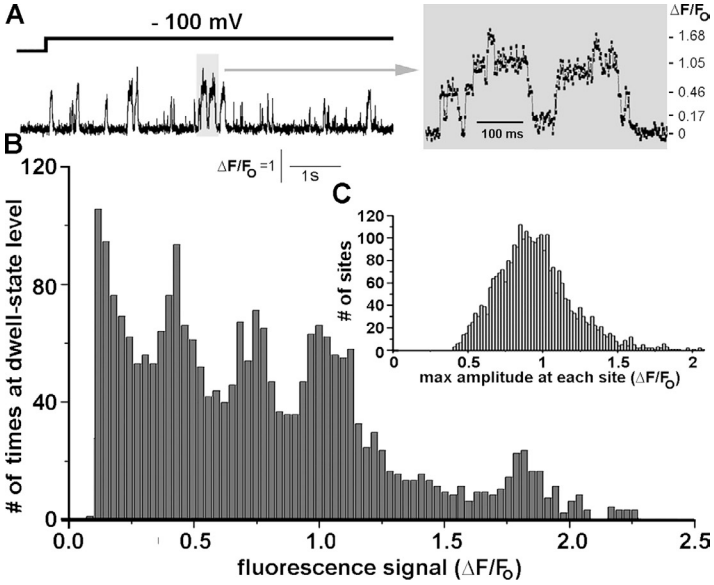

Figure 4. **SCCaFTs generated by Aβ1–42 display multiple Ca^{2+} flux levels.** (A) The trace at the left shows a representative record of SCCaFTs induced by Aβ1–42 oligomers, and the trace at the right shows the segment marked by the gray box on an expanded timescale. The bars indicate Ca^{2+} fluorescence levels ($\Delta F/F_0$) corresponding to different amplitude dwell states during SCCaFTs. (B) Distribution of dwell-state amplitude levels during Aβ1–42 SCCaFTs measured by visual inspection of traces from 76 pores selected from a single image record. (C) Distribution of the maximum SCCaFT amplitude observed at a given site generated by CellSpecks from an image sequence that encompassed 2,820 total sites. Data are representative of results from three or more image records obtained in each of four oocytes.

constants of 3.9 and 55 s (Fig. 6 B). The corresponding distribution of P_o showed a very wide range (Fig. 6 C), which could again be fitted by two exponential components. A majority of sites had low (<0.005) P_o values, but a few showed P_o values as high as 0.2. This spread in P_o primarily reflects differences in mean closed times among different pores and not differences in mean open times. After segregating the data into relatively low ($P_o < 0.02$) and high ($P_o \geq 0.02$) populations, we found only a roughly twofold difference in mean open time between these groups (respective values derived from single-exponential fits of 4.33 ± 0.20 and 19 ± 0.36 ms), whereas the mean closed times differed more than 10-fold (respective time constants 521 ± 55 and 4,271 ± 333 ms). Interestingly, the P_o of a pore correlated strongly with the amplitude of the largest event observed from that pore (Fig. 6 D).

Respective Ca^{2+} load contributed by Aβ1–42 pores with differing P_o

The toxicity of Aβ pores will presumably vary in proportion to the amount of Ca^{2+} that passes through them into the cytosol within a given time. Given the wide variation in permeability and gating properties among different pores, we were thus interested to determine which might represent the major toxic species: for example, whether a relatively small number of high P_o pores might contribute a greater fraction of the total cellular Ca^{2+} load than the more numerous low P_o pores. To obtain a relative estimate of the amount of Ca^{2+} entering the cell through a given pore in a fixed time, we analyzed fluorescence traces such as those in Fig. 5 B by integrating the local fluorescence signal over the time during which the pore was open ($\Delta F/F_o \times$ seconds). The blue bars in Fig. 7 A show the distribution of fluorescence

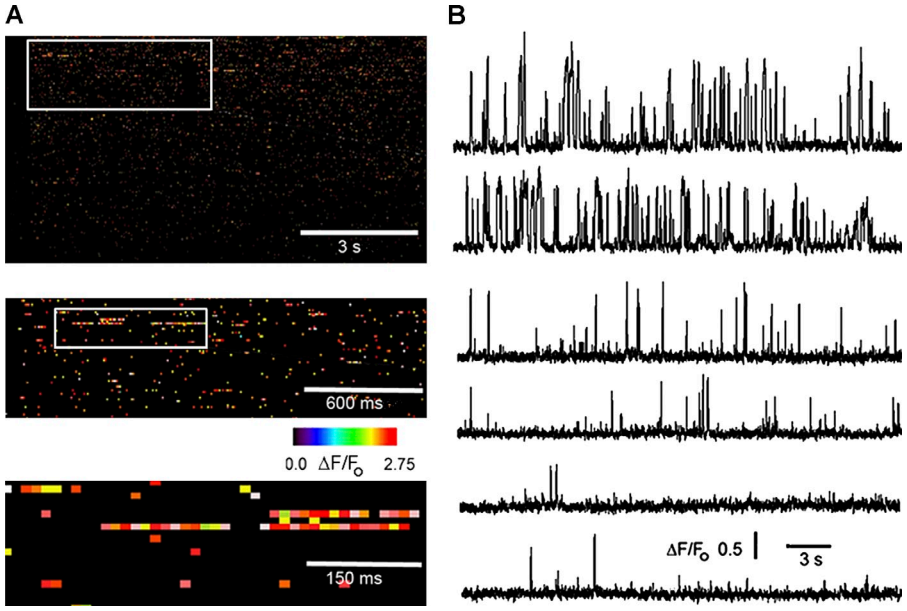

Figure 5. **Aβ1–42 pores display wide variability in kinetics and P_o.** (A) Channel-chip representation of the activity of Aβ1–42 pores. Pore openings (SCCaFTs) are represented as pseudocolored streaks, with warmer colors representing higher fluorescence signals, as indicated by the color bar; time runs from left to right. The top panel illustrates the activity of 170 different pores showing the highest P_o values among a total of 2,820 pores detected by CellSpecks within a single imaging frame (40 × 40 μm^2). Pores are depicted top to bottom in order of decreasing P_o. The bottom panels show consecutive expanded views of the regions marked by the white boxes. (B) Representative traces showing activity from six different pores, illustrating those with high (top two traces), medium (middle two traces), and low (bottom two traces) P_o.

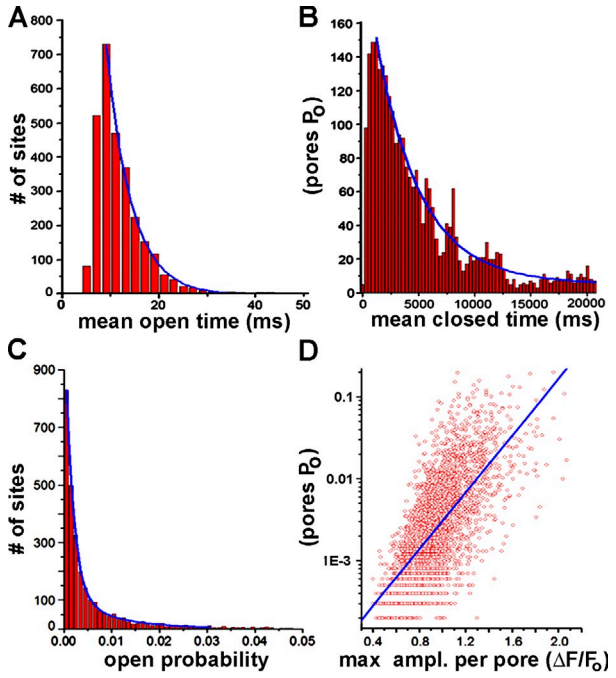

Figure 6. **Gating kinetics of Aβ1–42 pores.** (A) Distribution of mean open durations (SCCaFT durations) among the 2,820 pores. (B) Corresponding distribution of mean closed times (intervals between SCCaFTs). (C) Corresponding distribution of mean open probabilities (P_o; measured as proportion of time for which the fluorescence exceeded a threshold level above the baseline). (D) The P_o of pores strongly correlates with their calcium permeability. The scatter plot shows the P_o of pores as a function of the amplitude (ampl.) of the largest SCCaFT observed from that pore. (A–C) The blue curves are double exponential fits, with decay constants of 5.3 and 16.3 ms (A), 3.8 and 54 s (B), and 0.0017 and 0.0096 s (C). Data are representative of results from three or more image records obtained in each of four oocytes.

integrals for 768 pores within a representative imaging field, presented in rank order from those with the lowest integral at the left to those with the greatest integral at the right. To better visualize the fraction of the total Ca^{2+} load carried by the pores in relation to their respective fluorescence integrals, we further showed (Fig. 7 A, red curve) the cumulative contribution toward the normalized total Ca^{2+} load among the rank-ordered pores. This reveals a disproportionate contribution to the Ca^{2+} load among the population of Aβ pores. Analogous to the highly unequal distribution of incomes among US citizens, the top 5% of pores with greatest fluorescence integrals contribute about one half the total Ca^{2+} load. Fig. 7 shows the corresponding mean open probabilities (P_o; Fig. 7 B) and Ca^{2+} permeabilities (peak SCCaFT amplitude; Fig. 7 C) of the pores, ordered again by their fluorescence integrals to match Fig. 7 A. From these data, it is clear that the pores carrying a high toxic Ca^{2+} load are characterized primarily by their high P_o and that, although they also display on average a higher Ca^{2+} permeability, this factor plays a lesser role.

Time-dependent changes in Aβ1–42 pore properties

Visual inspection of image records indicated that the amplitudes of fluorescence signals at given sites increased progressively over several minutes after Aβ application. This is quantified in Fig. 7 (D–F), showing corresponding data from the same membrane region as in Fig. 7 (A–C) but obtained 10 min later (i.e., 30 min after beginning application of Aβ). Although the number of pores (SCCaFT sites) in the imaging field increased only slightly (from 768 to 805), the relative contributions among different pores to the cumulative Ca^{2+} load changed dramatically (Fig. 7 D). The proportion of pores with high fluorescence integrals (Fig. 7 D, blue bars) and high P_o (Fig. 7 E) was greater than at the earlier time point, such that the top 5% of pores now contributed almost 80% of the total Ca^{2+} load (Fig. 7 D, red curve), as compared with 50% 10 min earlier. Again, the P_o of a pore was the main factor in determining its contribution to the Ca^{2+} load (Fig. 7 E), whereas maximal SCCaFT amplitudes varied over only about a threefold range between pores (Fig. 7 F). Similar results were obtained in a total of four oocytes.

Discussion

Disruption of membrane integrity by soluble Aβ amyloids and consequent dysregulation of intracellular Ca^{2+} homeostasis are implicated as important pathogenic factors in AD (Demuro et al., 2005, 2010; Arispe et al., 2007; Kawahara, 2010; Camandola and Mattson, 2011). Although the specific molecular mechanisms remain controversial (Demuro et al., 2010), there is good evidence that Aβ oligomers create Ca^{2+}-permeable pores in the cell membrane (Arispe et al., 2007). The structure (Lal et al., 2007) and electrophysiological properties of these pores have been studied in artificial lipid membrane systems (Arispe et al., 2007) and in excised patches of neuronal membranes (Kawahara et al., 1997). Here, we used TIRF microscopy (Demuro and Parker, 2004b, 2005a) to resolve the permeation of Ca^{2+} through individual Aβ pores in the membrane of *Xenopus* oocytes. After bath application of Aβ1–42 oligomers, we observed that numerous localized transient hotspots of Ca^{2+} influx, which were dependent on the electrochemical driving force for influx of extracellular Ca^{2+}, were blocked by Zn^{2+} and closely resembled Ca^{2+} signals previously seen from single classical Ca^{2+}-permeable channels (Demuro and Parker, 2006). Moreover, we did not observe any spatially diffuse Zn^{2+}-insensitive Ca^{2+} elevations as expected if amyloid oligomers were to cause membrane thinning and reduction of the dielectric barrier to Ca^{2+} ion translocation (Sokolov et al., 2006); *Xenopus* oocytes lack endogenous channels reported to interact with Aβ amyloids (De Felice et al., 2007; Alberdi et al., 2010). Therefore, we conclude that the local Ca^{2+} transients (SCCaFTs) arise through openings of individual Aβ oligomer pores.

Thus, TIRF Ca^{2+} imaging provides a novel and powerful means to study the permeation and gating properties of amyloid membrane pores. Specific advantages include the incorporation of pores in a native cell membrane rather than an artificial lipid environment and the ability to simultaneously and independently monitor the activity of hundreds of pores within a small region of the cell membrane. This combination of high-throughput and single-molecule resolution is of particular importance because preparations of amyloid oligomers typically contain a mix of widely differing aggregation states (Demuro et al., 2010). Population measurements (e.g., whole-cell assays) yield no information regarding this diversity, and existing single-pore assays

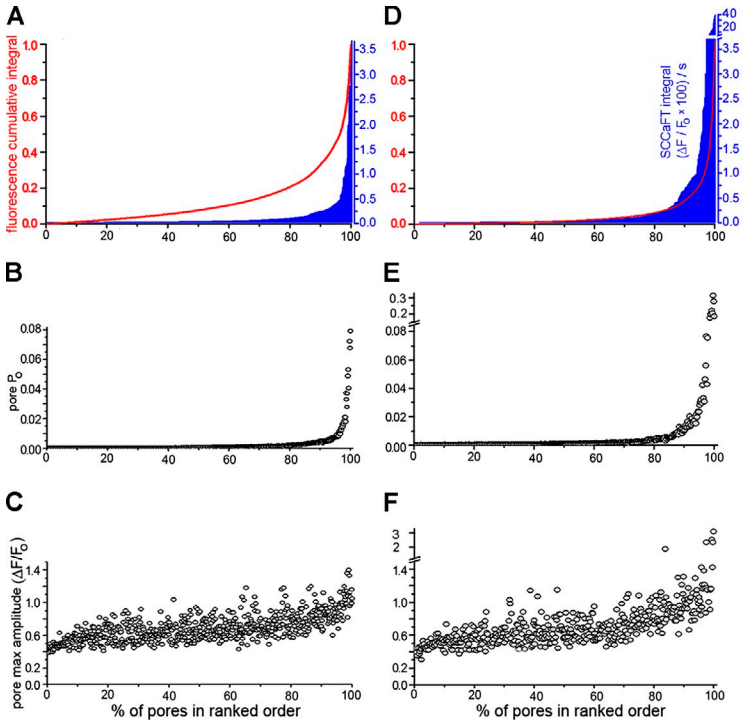

Figure 7. **Aβ1–42 pores with high open probabilities contribute disproportionately to the total cellular Ca^{2+} load.** The Ca^{2+} load contributed by a given pore was determined by integrating the area under the fluorescence trace (30-s duration), during which the fluorescence exceeded a threshold of 0.2 $\Delta F/F_o$. (A–F) The abscissa represents the number of pores within a 10 × 10–µm imaging field ranked in order of increasing Ca^{2+} load and normalized to 100%. (A–C) Data obtained 20 min after application of Aβ1–42 are shown. Plots of pore P_o (B) and amplitude of the largest SCCaFT observed at each site (C) on the same abscissa as in A are shown. (D–F) Corresponding analyses from the same membrane region as in A–C obtained 10 min later, showing a marked increase in proportion of pores contributing a high Ca^{2+} load. Blue bars (righthand ordinate; shown in A) show the Ca^{2+} load contributed by each individual pore expressed as an integral of the fluorescence signals during all SCCaFTs detected at that site. The curve (left ordinate; red) plots the cumulative contribution of pores toward the normalized total Ca^{2+} load.

(conductance measurements from bilayer systems) are laborious and provide only a very small sample size.

Concordant with a spectrum of oligomeric compositions, we observed enormous variation in functional properties between Aβ1–42 pores, even at the same time and within the same membrane region. Most dramatically, mean open probabilities spanned a nearly 1,000-fold range, and permeabilities (amplitudes of the largest Ca^{2+} fluorescence signal observed at each given site) varied as much as 10-fold ($\Delta F/F_o$ 0.2–2.0). Based on comparison with fluorescence signals recorded under comparable conditions from single acetylcholine receptor/channels of known Ca^{2+} conductance (Ca^{2+} current of ∼0.25 pA equivalent to $\Delta F/F_o$ 1.0; Demuro and Parker, 2005a), we estimate that Ca^{2+} currents through Aβ1–42 pores thus ranged between ∼0.05 and 0.5 pA at −100 mV, corresponding to Ca^{2+} conductances of ∼0.4–4 picosiemens assuming a reversal potential of 30 mV.

The maximal Ca^{2+} permeability of a pore correlated strongly with its P_o, and, similar to the transitions between conductance levels reported in electrophysiological recordings from Aβ pores in bilayers (Arispe et al., 1993, 2007), we observed frequent transitions between Ca^{2+} fluorescence dwell states during SCCaFTs. Several observations indicate that the multistep Ca^{2+} permeability levels did not arise because multiple Aβ1–42 pores colocalized within a region smaller than our limit of resolution; the stepwise behavior was seen even when the overall density of Aβ pores was very low, the amplitude levels were not distributed as integer multiples as expected if they represent the summated Ca^{2+} flux through multiple identical and independent pores, and we frequently observed apparently synchronous transitions across as many as four amplitude levels. Instead, we favor a mechanism wherein the multiple permeability levels represent different open states of a single pore, and the number of levels exhibited by a pore is determined by the number of Aβ peptides that have aggregated to form the pore. A recent study combining imaging of individual fluorescently labeled Aβ peptides into lipid bilayers together with conductance measurements led to a similar conclusion (Schauerte et al., 2010). Monomers and dimers were found to be nonconducting, whereas small oligomers (up to ∼14 mers) induced conductances of a few tens of picosiemens, and large aggregates (which formed only at high Aβ concentrations) gave conductances of hundreds of picosiemens. Schauerte et al. (2010) was unable to directly associate conductance measurements to individual fluorescent aggregates and instead segregated aggregation states into just three classes. Because the values from electrophysiological measurements are based on monovalent ion currents, it is not possible to make a direct comparison with our estimates of the specific Ca^{2+} conductance of Aβ pores. Nevertheless, our findings of a wide spectrum of permeability and gating properties point to a more nuanced continuum of properties within a population of Aβ pores that likely correspond to the class II morphological aggregates of Schauerte et al. (2010).

A related question is whether the Aβ oligomers that create Ca^{2+}-permeable pores are preformed in solution or aggregate after interaction of smaller precursors within the membrane. The available evidence suggests involvement of both processes. Consistent with rapid membrane incorporation of preestablished and functional oligomeric complexes, we had found that extracellular application of oligomeric Aβ resulted in rapid induction of membrane Ca^{2+} permeability, whereas monomers were ineffective (Demuro et al., 2005). On the other hand, Schauerte et al. (2010) described binding of individual fluorescently labeled Aβ monomers to lipid bilayers and subsequent appearance of ion-conducting oligomers at a rate much faster than the oligomerization rate (hours) in aqueous solution. Our finding that individual Aβ pores show progressive increases

in P_o and permeability over several minutes further supports the idea that pores already active in the membrane may grow and change their properties by continued accretion of monomers or small oligomers.

SCCaFTs arising from Aβ pores remained at fixed locations over several minutes. This greatly simplified analysis but is surprising because free diffusion of proteins in the lipid membrane would be expected to result in clearly detectable movements of several micrometers (Demuro and Parker, 2005a). We do not believe that the immotility of pores arose through mechanical interaction with the cover glass because a similar lack of motility was evident in oocytes with intact vitelline envelope. Instead, Aβ may bind to some static cytoskeletal structure.

Our results were obtained using *Xenopus* oocytes, and it remains to be determined how closely the actions of Aβ on this model cell system replicate those on neuronal membranes. Moreover, it is not clear how the progressive changes in gating and permeability that we observe over a timescale of minutes may relate to the progression of AD over years, during which time neurons are continually exposed to low but rising concentrations of soluble Aβ in the cerebrospinal fluid. Nevertheless, we speculate that the initial evolution of the disease may involve formation of small-conductance, low P_o pores that, although not immediately triggering cell death, produce chronic pathological cell stress. A tipping point may then be reached when a sustainable level of Ca^{2+} influx through these pores is abruptly exceeded by the appearance of even a few high-conductance, high P_o pores that contribute a disproportionately large Ca^{2+} load.

In summary, our application of high-resolution TIRF imaging provides strong support for a mechanism whereby Aβ amyloid oligomers form intrinsic Ca^{2+}-permeable pores in the cell membrane and enables massively parallel characterization of the permeation and gating properties of thousands of pores. Our results reveal an enormous range in activities that may reflect concentration—and time dependent—differences in stoichiometries of Aβ pores and suggest a mechanism wherein continued aggregation of oligomers leads to the formation of highly active high-permeability pores that may play a disproportionate cytotoxic role in the pathogenesis of AD. Moreover, our single-channel Ca^{2+} imaging approach would be equally applicable to studies of numerous other amyloid-related diseases, including Huntington's, Parkinson's, and prion disease, in which increased membrane Ca^{2+} permeability is implicated as a major pathological mechanism (Demuro et al., 2005).

Materials and methods

Preparation and characterization of Aβ1–42 oligomers

Soluble oligomers were prepared by dissolving 0.5 mg of human recombinant Aβ1–42 peptide (hexafluoroisopropanol pretreated; rPeptide) in 20 µl of freshly prepared DMSO and were quickly diluted with 480 µl of double-distilled water in a siliconized Eppendorf tube. After a 10-min sonication, samples were incubated at room temperature for 10 min and then centrifuged for 15 min at 14,000 *g*. The supernatant fraction was transferred to a new siliconized tube and stirred at 500 rpm using a Teflon-coated microstir bar for 8–48 h at room temperature. Aliquots were taken at intervals and were assayed by pipette application to voltage-clamped oocytes at a final bath concentration of 1 µg/ml. Membrane currents were recorded 30 min after application in response to hyperpolarization from 0 to −100 mV. Aβ preparations incubated for <6 h evoked little or no current, indicating that the monomeric peptide was ineffective at inducing membrane Ca^{2+} permeability. Preparations that evoked currents ≥1 µA were used immediately for TIRF imaging or were stored at −20°C before use (Demuro et al., 2005). Aβ1–42 samples were further characterized by Western blot analysis (Kayed et al., 2010). Samples containing 4 µg Aβ1–42 were diluted in SDS treatment buffer, boiled for 5 min, and separated on a 4–20% Tris-HCl gel (Bio-Rad Laboratories) at 4°C for 2 h at 85 V. Proteins were transferred onto a nitrocellulose membrane, which was then blocked for 1 h in 5% nonfat dry milk in TBS/Tween 20 buffer. The membranes were probed with the mouse monoclonal anti-Aβ antibody 6E10 (0.1 µg/ml; Sigma-Aldrich), and the conformation-specific polyclonal antibody OC (0.4 µg/ml; a gift from C. Glabe, University of California, Irvine, Irvine, CA) overnight at 4°C. The membranes were then incubated with anti–rabbit IgG conjugated with HRP (1:10,000) for 1 h at room temperature. Blots were developed with a chemiluminescence kit (SuperSignal West Pico; Thermo Fisher Scientific).

Oocyte preparation and electrophysiology

Experiments were performed on defolliculated stage VI oocytes obtained from *Xenopus*. Oocytes were injected ∼1 h before imaging with fluo-4 dextran (molecular mass of ∼10 kD and Ca^{2+} affinity of ∼3 µM) to a final intracellular concentration of ∼40 µM. For TIRF microscopy experiments, oocytes were placed in a hypertonic solution (200 mM K aspartate, 20 mM KCl, 1 mM $MgCl_2$, 10 mM EGTA, and 10 mM Hepes, pH 7.2) at 4°C to shrink them so that the vitelline envelope could be manually torn apart and removed using fine forceps. Oocytes were then placed animal hemisphere down in a chamber whose bottom is formed by a fresh ethanol-washed microscope cover glass (type-545-M; Thermo Fisher Scientific) and were bathed in Ringer's solution (110 mM NaCl, 1.8 mM $CaCl_2$, 2 mM KCl, and 5 mM Hepes, pH 7.2) at room temperature (∼23°C) continually exchanged at a rate of ∼0.5 ml/min^{-1} by a gravity-fed superfusion system. The membrane potential was clamped at a holding potential of 0 mV using a two-electrode voltage clamp (Gene Clamp 500; Molecular Devices) and was stepped to more negative potentials (−100 mV unless otherwise indicated) when imaging Ca^{2+} flux through amyloid pores to increase the driving force for Ca^{2+} entry in to the cytosol. Solutions containing Aβ42 oligomers were delivered from a glass pipette with a tip diameter of ∼30 µm positioned near the edge of the membrane footprint of the oocyte membrane on the cover glass.

TIRF microscopy, image acquisition, and processing

Imaging was accomplished by using a custom-built TIRF microscope system based around a microscope (IX70; Olympus) equipped with a 60× TIRF microscopy objective (1.45 NA; Olympus; Demuro and Parker, 2005b). Fluorescence excited by a 488-nm laser was imaged using an electron-multiplied charge-coupled device camera (Cascade 128+; Roper Scientific) at full resolution (128 × 128 pixel; 1 pixel = 0.33 µm at the specimen) at a rate of 500 s^{-1}. Image data were acquired using the MetaMorph software package (Universal Imaging) and were black-level corrected by subtracting the camera offset. To compensate for differential time-dependent changes in basal fluorescence across different locations in the image field, a strongly smoothed (10 × 10–pixel Gaussian blur) copy of each frame was calculated to create a running baseline (F_0) image. The raw image stack was then divided, frame by frame, by the smoothed copy to create a baseline-corrected pseudoratio stack in which each pixel represents localized differences in fluorescence relative to the spatially averaged baseline fluorescence ($\Delta F/F_0$). In initial experiments, data were analyzed manually using MetaMorph to visually identify sites of pore activity, and traces of fluorescence versus time such as those in Figs. 2–5 were obtained as the maximum pixel intensity within fixed 3 × 3–pixel (∼1 × 1 µm) regions of interest centered on putative pore locations. Fluorescence measurements were not confounded by movement of Aβ pores, as tracking the centroid locations of SCCaFTs with subpixel resolution revealed only slight random deviations throughout the imaging record (SD typically <0.3 pixel), which are negligible in comparison with the size of the regions of interest used to measure fluorescence intensities. The maximum observed fluorescence signals were small (maximum $\Delta F/F_o$ <2.0) in comparison with the full dynamic range of fluo-4 ($\Delta F/F_o$ >30 in saturating Ca^{2+}) and are thus expected to be linearly proportional to Ca^{2+} flux.

Event detection algorithm and automated data analysis (CellSpecks)

TIRF microscopy recordings produce large (128 × 128 pixel × 15,000 frame) image stacks, which can represent the activity of >1,000 discrete Aβ pores. Thus, it was extremely laborious to compile and analyze population data by visual inspection, and we did not find existing software, including GMimPro and SparkMaster (Mashanov and Molloy, 2007; Picht et al., 2007),

adequate for our purposes. Accordingly, we developed a Java-based program (CellSpecks) to identify active sites, generate idealized traces of pore gating, and derive parameters, including mean open and closed times and open probabilities as presented in Figs. 6 and 7. CellSpecks is coded in Java and accepts image files in MetaMorph stack format or using Sun Java standard libraries for opening directories of sequential images. Each frame is converted into a new 2D array and stored as a stack object in memory. The steps described in the next sections are then performed to identify fluorescence signals, associate these with pore locations, and output final data statistics.

Fluorescence thresholding. For each pixel, a 1D array of intensity values over the time is created and is corrected for baseline drift by subtraction of a heavily smoothed copy formed by filtering with a boxcar mean 51 frames in length. The modal value (most commonly observed value) of the resulting array is then taken as the baseline, and an estimate of baseline noise is calculated as the SD of only those source values that fall below the mode. A value of 2.5 times the negative SDs above the mode was selected as the noise threshold to minimize false positives, and a new stack is created in which all pixel values below the threshold are set to 0, and those above threshold are set to their original values relative to the mode.

Event detection. The event detection process is based on an object-oriented programming paradigm. For each pixel, a new 3D array (x,y,t) of event-part object pointers is generated to represent the pixel in space and time. Each event-part object contains the intensity value at that location in time as well as pointers to event-parts above, below, left, right, and before and after (in time) the current pixel. When these event-parts are loaded into each other's pointers, contiguous signal pixels are then linked to each other and bounded by null pointers to nonsignal pixels. Events are built from these 3D groups of contiguous signal pixels by scanning the stack and recursively linking all contiguous event parts to a single event object (SCCaFT). At the end of this process, a list of all event locations in the stack is generated. After constructing a list of events, CellSpecks performs a series of steps to generate a list of pore locations.

Channel attribution. The events are then analyzed one by one and assigned to a designated pore location. To facilitate the location of pores, a weight array, $g(x,y)$, is generated as a 2D array containing the sum of pixel values from the original stack over time. Local maxima are interpreted as likely pore locations and are used to create an initial list of putative pore objects. Events are then linked to pores one by one, either to the closest known pore or to a new pore location. Because the coordinates of a pore are dynamically generated from their constituent events, events early in the stack could bias the location of pores to which subsequent nearby larger events may be assigned. The algorithm avoids this problem by seeding the list of pores with the locations of larger events (whose fluorescence spread over a larger area and could therefore be more flexibly associated) regardless of their order, so that they are assigned their own putative pore locations at the outset. Whether or not an event is added to the existing pore list depends on two criteria. The first is binary overlap verification that checks whether or not the coordinates of the event and pore in consideration when rounded to the nearest pixel in space are equal. Event locations are calculated from their constituent event parts using a mean of the event-part coordinates weighted by intensity. The coordinate for the location of the pore is than calculated using a mean of the coordinates of the pore's constituent events weighted by each event's total intensity, calculated as the sum of the intensity measured in all the pixels involved in space and time. The second criterion for event-pore association takes into consideration the relative intensity, Ir, of the event's pixels at the assigned pore location over the duration of the event. Ir is calculated as the ratio between the sums of the intensity of each pixel over the duration of the events versus the maximum intensity measured at this location. The relative intensity of an event at the center of the pore multiplied by the inverse of distance between the event and pore centers must be >0.2, a threshold value empirically determined for our experimental conditions.

Events that do not fulfil either of these criteria are assigned to new pore locations. Finally, putative pore locations from the initial list that are not associated with any events are discarded. By the end of the detection and attribution processes, a final list of designated pore locations has been produced, and each location is associated with a list of linked events.

Data visualization, analysis, and export. The list of events associated with each pore location is used to derive distributions of pore open and closed times (i.e., event durations and inter-event intervals), from which population statistics are then calculated. A graphical user interface allows on-screen viewing of raw and processed data (e.g., intermediate stack, baseline, signal, and noise information). Clicking on a map of locations brings up plots as these values as functions of time, and sampling can be modified to select a mean or maximum of pixel values over a user-specified region of interest. Data (including individual measurements of event durations, intervals, and fluorescence amplitudes together with population measurements of mean pore open/closed times, P_o, and mean fluorescence) are exported as ASCII text files.

Materials

Fluo-4 dextran was purchased from Invitrogen, and human Aβ1−42 peptide was purchased from Millipore and rPeptide. gsmtx-4 was a gift from F. Sachs (University at Buffalo, Buffalo, NY). All other reagents and antibodies were purchased from Sigma-Aldrich.

We are grateful to Anna Pensalfini for assistance in performing Western blot analyses of oligomer preparations. We thank Dr. Frederick Sachs for kindly providing gsmtx-4 and Dr. Charles Glabe for the OC antibody.

This work was supported by National Institutes of Health grants GM48071 (to I. Parker) and P50-AG16573 (to A. Demuro).

Submitted: 26 April 2011
Accepted: 26 September 2011

References

Alberdi, E., M.V. Sánchez-Gómez, F. Cavaliere, A. Pérez-Samartín, J.L. Zugaza, R. Trullas, M. Domercq, and C. Matute. 2010. Amyloid beta oligomers induce Ca^{2+} dysregulation and neuronal death through activation of ionotropic glutamate receptors. *Cell Calcium*. 47:264–272. http://dx.doi.org/10.1016/j.ceca.2009.12.010

Arispe, N., H.B. Pollard, and E. Rojas. 1993. Giant multilevel cation channels formed by Alzheimer disease amyloid beta-protein [A beta P-(1-40)] in bilayer membranes. *Proc. Natl. Acad. Sci. USA*. 90:10573–10577. http://dx.doi.org/10.1073/pnas.90.22.10573

Arispe, N., H.B. Pollard, and E. Rojas. 1996. Zn^{2+} interaction with Alzheimer amyloid beta protein calcium channels. *Proc. Natl. Acad. Sci. USA*. 93:1710–1715. http://dx.doi.org/10.1073/pnas.93.4.1710

Arispe, N., J.C. Diaz, and O. Simakova. 2007. Abeta ion channels. Prospects for treating Alzheimer's disease with Abeta channel blockers. *Biochim. Biophys. Acta*. 1768:1952–1965. http://dx.doi.org/10.1016/j.bbamem.2007.03.014

Bode, F., F. Sachs, and M.R. Franz. 2001. Tarantula peptide inhibits atrial fibrillation. *Nature*. 409:35–36. http://dx.doi.org/10.1038/35051165

Bourinet, E., F. Fournier, J. Nargeot, and P. Charnet. 1992. Endogenous *Xenopus*-oocyte Ca-channels are regulated by protein kinases A and C. *FEBS Lett.* 299:5–9. http://dx.doi.org/10.1016/0014-5793(92)80087-W

Bucciantini, M., E. Giannoni, F. Chiti, F. Baroni, L. Formigli, J. Zurdo, N. Taddei, G. Ramponi, C.M. Dobson, and M. Stefani. 2002. Inherent toxicity of aggregates implies a common mechanism for protein misfolding diseases. *Nature*. 416:507–511. http://dx.doi.org/10.1038/416507a

Cahalan, M.D. 2009. STIMulating store-operated $Ca^{(2+)}$ entry. *Nat. Cell Biol.* 11:669–677. http://dx.doi.org/10.1038/ncb0609-669

Camandola, S., and M.P. Mattson. 2011. Aberrant subcellular neuronal calcium regulation in aging and Alzheimer's disease. *Biochim. Biophys. Acta*. 1813:965–973. http://dx.doi.org/10.1016/j.bbamcr.2010.10.005

Capone, R., F.G. Quiroz, P. Prangkio, I. Saluja, A.M. Sauer, M.R. Bautista, R.S. Turner, J. Yang, and M. Mayer. 2009. Amyloid-beta-induced ion flux in artificial lipid bilayers and neuronal cells: Resolving a controversy. *Neurotox. Res.* 16:1–13. http://dx.doi.org/10.1007/s12640-009-9033-1

Cras, P., M. Kawai, D. Lowery, P. Gonzalez-DeWhitt, B. Greenberg, and G. Perry. 1991. Senile plaque neurites in Alzheimer disease accumulate amyloid precursor protein. *Proc. Natl. Acad. Sci. USA*. 88:7552–7556. http://dx.doi.org/10.1073/pnas.88.17.7552

De Felice, F.G., P.T. Velasco, M.P. Lambert, K. Viola, S.J. Fernandez, S.T. Ferreira, and W.L. Klein. 2007. Abeta oligomers induce neuronal oxidative stress through an N-methyl-D-aspartate receptor-dependent mechanism that is blocked by the Alzheimer drug memantine. *J. Biol. Chem.* 282:11590–11601. http://dx.doi.org/10.1074/jbc.M607483200

Demuro, A., and I. Parker. 2003. Optical single-channel recording: imaging Ca^{2+} flux through individual N-type voltage-gated channels expressed in *Xenopus* oocytes. *Cell Calcium*. 34:499–509. http://dx.doi.org/10.1016/S0143-4160(03)00154-4

Demuro, A., and I. Parker. 2004a. Imaging single-channel calcium microdomains by total internal reflection microscopy. *Biol. Res.* 37:675–679. http://dx.doi.org/10.4067/S0716-97602004000400025

Demuro, A., and I. Parker. 2004b. Imaging the activity and localization of single voltage-gated $Ca^{(2+)}$ channels by total internal reflection fluorescence microscopy. *Biophys. J.* 86:3250–3259. http://dx.doi.org/10.1016/S0006-3495(04)74373-8

Demuro, A., and I. Parker. 2005a. "Optical patch-clamping": Single-channel recording by imaging Ca2+ flux through individual muscle acetylcholine receptor channels. *J. Gen. Physiol.* 126:179–192. http://dx.doi.org/10.1085/jgp.200509331

Demuro, A., and I. Parker. 2005b. Optical single-channel recording: Imaging Ca^{2+} flux through individual ion channels with high temporal and spatial resolution. *J. Biomed. Opt.* 10:11002. http://dx.doi.org/10.1117/1.1846074

Demuro, A., and I. Parker. 2006. Imaging single-channel calcium microdomains. *Cell Calcium*. 40:413–422. http://dx.doi.org/10.1016/j.ceca.2006.08.006

Demuro, A., E. Mina, R. Kayed, S.C. Milton, I. Parker, and C.G. Glabe. 2005. Calcium dysregulation and membrane disruption as a ubiquitous neurotoxic mechanism of soluble amyloid oligomers. *J. Biol. Chem.* 280:17294–17300. http://dx.doi.org/10.1074/jbc.M500997200

Demuro, A., I. Parker, and G.E. Stutzmann. 2010. Calcium signaling and amyloid toxicity in Alzheimer disease. *J. Biol. Chem.* 285:12463–12468. http://dx.doi.org/10.1074/jbc.R109.080895

Deshpande, A., E. Mina, C. Glabe, and J. Busciglio. 2006. Different conformations of amyloid beta induce neurotoxicity by distinct mechanisms in human cortical neurons. *J. Neurosci.* 26:6011–6018. http://dx.doi.org/10.1523/JNEUROSCI.1189-06.2006

Durell, S.R., H.R. Guy, N. Arispe, E. Rojas, and H.B. Pollard. 1994. Theoretical models of the ion channel structure of amyloid beta-protein. *Biophys. J.* 67:2137–2145. http://dx.doi.org/10.1016/S0006-3495(94)80717-9

Glabe, C.G. 2004. Conformation-dependent antibodies target diseases of protein misfolding. *Trends Biochem. Sci.* 29:542–547. http://dx.doi.org/10.1016/j.tibs.2004.08.009

Hardy, J.A., and G.A. Higgins. 1992. Alzheimer's disease: the amyloid cascade hypothesis. *Science*. 256:184–185. http://dx.doi.org/10.1126/science.1566067

Hertel, C., E. Terzi, N. Hauser, R. Jakob-Rotne, J. Seelig, and J.A. Kemp. 1997. Inhibition of the electrostatic interaction between beta-amyloid peptide and membranes prevents beta-amyloid-induced toxicity. *Proc. Natl. Acad. Sci. USA*. 94:9412–9416. http://dx.doi.org/10.1073/pnas.94.17.9412

Inoue, S. 2008. In situ Abeta pores in AD brain are cylindrical assembly of Abeta protofilaments. *Amyloid*. 15:223–233. http://dx.doi.org/10.1080/13506120802524858

Jang, H., J. Zheng, R. Lal, and R. Nussinov. 2008. New structures help the modeling of toxic amyloidbeta ion channels. *Trends Biochem. Sci.* 33:91–100. http://dx.doi.org/10.1016/j.tibs.2007.10.007

Jarrett, J.T., and P.T. Lansbury Jr. 1993. Seeding "one-dimensional crystallization" of amyloid: A pathogenic mechanism in Alzheimer's disease and scrapie? *Cell*. 73:1055–1058. http://dx.doi.org/10.1016/0092-8674(93)90635-4

Jensen, M., T. Hartmann, B. Engvall, R. Wang, S.N. Uljon, K. Sennvik, J. Näslund, F. Muehlhauser, C. Nordstedt, K. Beyreuther, and L. Lannfelt. 2000. Quantification of Alzheimer amyloid beta peptides ending at residues 40 and 42 by novel ELISA systems. *Mol. Med.* 6:291–302.

Kagan, B.L., R. Azimov, and R. Azimova. 2004. Amyloid peptide channels. *J. Membr. Biol.* 202:1–10. http://dx.doi.org/10.1007/s00232-004-0709-4

Kawahara, M. 2010. Neurotoxicity of β-amyloid protein: oligomerization, channel formation, and calcium dyshomeostasis. *Curr. Pharm. Des.* 16:2779–2789.

Kawahara, M., N. Arispe, Y. Kuroda, and E. Rojas. 1997. Alzheimer's disease amyloid beta-protein forms $Zn^{(2+)}$-sensitive, cation-selective channels across excised membrane patches from hypothalamic neurons. *Biophys. J.* 73:67–75. http://dx.doi.org/10.1016/S0006-3495(97)78048-2

Kayed, R., E. Head, J.L. Thompson, T.M. McIntire, S.C. Milton, C.W. Cotman, and C.G. Glabe. 2003. Common structure of soluble amyloid oligomers implies common mechanism of pathogenesis. *Science*. 300:486–489. http://dx.doi.org/10.1126/science.1079469

Kayed, R., I. Canto, L. Breydo, S. Rasool, T. Lukacsovich, J. Wu, R. Albay III, A. Pensalfini, S. Yeung, E. Head, et al. 2010. Conformation dependent monoclonal antibodies distinguish different replicating strains or conformers of prefibrillar Aβ oligomers. *Mol. Neurodegener.* 5:57. http://dx.doi.org/10.1186/1750-1326-5-57

Kim, W., and M.H. Hecht. 2005. Sequence determinants of enhanced amyloidogenicity of Alzheimer Abeta42 peptide relative to Abeta40. *J. Biol. Chem.* 280:35069–35076. http://dx.doi.org/10.1074/jbc.M505763200

Lal, R., H. Lin, and A.P. Quist. 2007. Amyloid beta ion channel: 3D structure and relevance to amyloid channel paradigm. *Biochim. Biophys. Acta*. 1768:1966–1975. http://dx.doi.org/10.1016/j.bbamem.2007.04.021

Lashuel, H.A., D. Hartley, B.M. Petre, T. Walz, and P.T. Lansbury Jr. 2002. Neurodegenerative disease: amyloid pores from pathogenic mutations. *Nature*. 418:291. http://dx.doi.org/10.1038/418291a

Lemere, C.A., J.K. Blusztajn, H. Yamaguchi, T. Wisniewski, T.C. Saido, and D.J. Selkoe. 1996. Sequence of deposition of heterogeneous amyloid beta-peptides and APO E in Down syndrome: Implications for initial events in amyloid plaque formation. *Neurobiol. Dis.* 3:16–32. http://dx.doi.org/10.1006/nbdi.1996.0003

Lin, H., R. Bhatia, and R. Lal. 2001. Amyloid beta protein forms ion channels: Implications for Alzheimer's disease pathophysiology. *FASEB J.* 15:2433–2444. http://dx.doi.org/10.1096/fj.01-0377com

Mashanov, G.I., and J.E. Molloy. 2007. Automatic detection of single fluorophores in live cells. *Biophys. J.* 92:2199–2211. http://dx.doi.org/10.1529/biophysj.106.081117

Mason, R.P., R.F. Jacob, M.F. Walter, P.E. Mason, N.A. Avdulov, S.V. Chochina, U. Igbavboa, and W.G. Wood. 1999. Distribution and fluidizing action of soluble and aggregated amyloid beta-peptide in rat synaptic plasma membranes. *J. Biol. Chem.* 274:18801–18807. http://dx.doi.org/10.1074/jbc.274.26.18801

Mattson, M.P., B. Cheng, D. Davis, K. Bryant, I. Lieberburg, and R.E. Rydel. 1992. beta-Amyloid peptides destabilize calcium homeostasis and render human cortical neurons vulnerable to excitotoxicity. *J. Neurosci.* 12:376–389.

Miledi, R., and I. Parker. 1984. Chloride current induced by injection of calcium into *Xenopus* oocytes. *J. Physiol.* 357:173–183.

Picht, E., A.V. Zima, L.A. Blatter, and D.M. Bers. 2007. SparkMaster: Automated calcium spark analysis with ImageJ. *Am. J. Physiol. Cell Physiol.* 293:C1073–C1081. http://dx.doi.org/10.1152/ajpcell.00586.2006

Pollard, H.B., E. Rojas, and N. Arispe. 1993. A new hypothesis for the mechanism of amyloid toxicity, based on the calcium channel activity of amyloid beta protein (A beta P) in phospholipid bilayer membranes. *Ann. NY Acad. Sci.* 695:165–168. http://dx.doi.org/10.1111/j.1749-6632.1993.tb23046.x

Quist, A., I. Doudevski, H. Lin, R. Azimova, D. Ng, B. Frangione, B. Kagan, J. Ghiso, and R. Lal. 2005. Amyloid ion channels: A common structural link for protein-misfolding disease. *Proc. Natl. Acad. Sci. USA*. 102:10427–10432. http://dx.doi.org/10.1073/pnas.0502066102

Rhee, S.K., A.P. Quist, and R. Lal. 1998. Amyloid beta protein-(1-42) forms calcium-permeable, Zn2+-sensitive channel. *J. Biol. Chem.* 273:13379–13382. http://dx.doi.org/10.1074/jbc.273.22.13379

Rovira, C., N. Arbez, and J. Mariani. 2002. Abeta(25-35) and Abeta(1-40) act on different calcium channels in CA1 hippocampal neurons. *Biochem. Biophys. Res. Commun.* 296:1317–1321. http://dx.doi.org/10.1016/S0006-291X(02)02072-7

Schauerte, J.A., P.T. Wong, K.C. Wisser, H. Ding, D.G. Steel, and A. Gafni. 2010. Simultaneous single-molecule fluorescence and conductivity studies reveal distinct classes of Abeta species on lipid bilayers. *Biochemistry*. 49:3031–3039. http://dx.doi.org/10.1021/bi901444w

Shankar, G.M., S. Li, T.H. Mehta, A. Garcia-Munoz, N.E. Shepardson, I. Smith, F.M. Brett, M.A. Farrell, M.J. Rowan, C.A. Lemere, et al. 2008. Amyloid-beta protein dimers isolated directly from Alzheimer's brains impair synaptic plasticity and memory. *Nat. Med.* 14:837–842. http://dx.doi.org/10.1038/nm1782

Smith, I.F., and I. Parker. 2009. Imaging the quantal substructure of single IP3R channel activity during Ca2+ puffs in intact mammalian cells. *Proc. Natl. Acad. Sci. USA*. 106:6404–6409. http://dx.doi.org/10.1073/pnas.0810799106

Sokolov, Y., J.A. Kozak, R. Kayed, A. Chanturiya, C. Glabe, and J.E. Hall. 2006. Soluble amyloid oligomers increase bilayer conductance by altering dielectric structure. *J. Gen. Physiol.* 128:637–647. http://dx.doi.org/10.1085/jgp.200609533

Walsh, D.M., I. Klyubin, J.V. Fadeeva, W.K. Cullen, R. Anwyl, M.S. Wolfe, M.J. Rowan, and D.J. Selkoe. 2002. Naturally secreted oligomers of amyloid beta protein potently inhibit hippocampal long-term potentiation in vivo. *Nature*. 416:535–539. http://dx.doi.org/10.1038/416535a

Wang, H.Y., D.H. Lee, M.R. D'Andrea, P.A. Peterson, R.P. Shank, and A.B. Reitz. 2000. beta-Amyloid(1-42) binds to alpha7 nicotinic acetylcholine receptor with high affinity. Implications for Alzheimer's disease pathology. *J. Biol. Chem.* 275:5626–5632. http://dx.doi.org/10.1074/jbc.275.8.5626

Weber, W.M. 1999. Endogenous ion channels in oocytes of *xenopus laevis*: Recent developments. *J. Membr. Biol.* 170:1–12. http://dx.doi.org/10.1007/s002329900532